

See discussions, stats, and author profiles for this publication at: <https://www.researchgate.net/publication/41806057>

Effect of charge distribution on RDX adsorption in IRMOF-10

ARTICLE *in* LANGMUIR · MARCH 2010

Impact Factor: 4.46 · DOI: 10.1021/la9039013 · Source: PubMed

CITATIONS

21

READS

35

10 AUTHORS, INCLUDING:



[Andrea Michalkova](#)

45 PUBLICATIONS 664 CITATIONS

[SEE PROFILE](#)



[Tetyana Petrova](#)

Jackson State University

11 PUBLICATIONS 114 CITATIONS

[SEE PROFILE](#)



[Khorgolkhuu Odbadrakh](#)

Joint Institute for Computational Sciences, ...

34 PUBLICATIONS 106 CITATIONS

[SEE PROFILE](#)



[James P Lewis](#)

West Virginia University

90 PUBLICATIONS 2,800 CITATIONS

[SEE PROFILE](#)

Effect of Charge Distribution on RDX Adsorption in IRMOF-10

Ruichang Xiong,[†] David J. Keffer,^{*,†} Miguel Fuentes-Cabrera,[‡] Donald M. Nicholson,[§] Andrea Michalkova,^{||} Tetyana Petrova,^{||} Jerzy Leszczynski,^{||} Khorgolkhuu Odbadrakh,[⊥] Bryant L. Doss,[⊥] and James P. Lewis[⊥]

[†]Department of Chemical and Biomolecular Engineering, University of Tennessee, Knoxville, Tennessee 37996,

[‡]Joint Institute for Computational Science, University of Tennessee and Center for Nanophase Materials Sciences, Oak Ridge National Laboratory, Oak Ridge, Tennessee 37830, [§]Computer Science and Mathematics Division, Oak Ridge National Laboratory, Oak Ridge, Tennessee 37830, ^{||}Interdisciplinary Nanotoxicity Center, Jackson State University, Jackson, Mississippi 39217, and [⊥]Department of Physics, West Virginia University, Morgantown, West Virginia 26506

Received October 14, 2009. Revised Manuscript Received February 15, 2010

Quantum mechanical (QM) calculations, classical grand canonical Monte Carlo (GCMC) simulations, and classical molecular dynamics (MD) simulations are performed to test the effect of charge distribution on hexahydro-1,3,5-trinitro-1,3,5-triazine (RDX) adsorption and diffusion in IRMOF-10. Several different methods for mapping QM electron distributions onto atomic point charges are explored, including the electrostatic potential (ESP) method, Mulliken population analysis, Löwdin population analysis, and natural bond orbital analysis. Classical GCMC and MD simulations of RDX in IRMOF-10 are performed using 15 combinations of charge sources of RDX and IRMOF-10. As the charge distributions vary, interaction potential energies, the adsorption loading, and the self-diffusivities are significantly different. None of the 15 combinations are able to quantitatively capture the dependence of the energy of adsorption on local configuration of RDX as observed in the QM calculations. We observe changes in the charge distributions of RDX and IRMOF-10 with the introduction of an RDX molecule into the cage. We also observe a large dispersion contribution to the interaction energy from QM calculations that is not reproduced in the classical simulations, indicating that the source of discrepancy may not lie exclusively with the assignment of charges.

1. Introduction

The detection of explosive molecules remains a challenge due to the low vapor pressure of explosive compounds, which in a threat situation may be present in the air at only parts per trillion concentrations.¹ To enhance the sensitivity and selectivity of detective sensors, an efficient preconcentration system is crucial for the trace detection process. The role of a preconcentrator is to trap a sufficient quantity of explosive molecules for detection by the sensor element from an extremely low concentration in the local air. To facilitate continuous operation, the preconcentrator needs to be able to desorb the trapped molecules easily, specifically at room temperature. Therefore, desirable features of a preconcentrator are high sensitivity, selectivity, and reversibility.^{2,3} Currently no preconcentrators available meet the above requirements. Conventional bulky preconcentrators have slow response times. Recent microfabricated preconcentrators can enhance sensitivity alone but still are not ideal.³

However, the fast development of nanotechnology provides an opportunity for developing an ideal preconcentrator. Metal-organic frameworks (MOFs) are a new class of nanoporous materials first synthesized by Yaghi and co-workers^{4–6} and have been evaluated for many tasks, including their ability to adsorb

methane^{6,7} and hydrogen.^{8–10} Because of their unique measured and calculated properties, such as large internal surface area, high thermal stability, high porosity, and tailorable pore size and chemistry, MOFs have been recently considered for their potential to preconcentrate explosive compounds.^{11,12} Ni et al.¹² have shown that IRMOF-1 is an effective selective preconcentrator when adsorbing dimethyl methylphosphonate (DMMP). In our previous work,¹³ we evaluated the ability of IRMOF-1, an isorecticular metal-organic framework (IRMOF), to adsorb the highly energetic explosive hexahydro-1,3,5-trinitro-1,3,5-triazine (RDX, CAS No. 121-82-4). The structure of RDX is shown in Figure 1. In order to understand how the structure of the IRMOF impacts the adsorption isotherm and thus the selectivity, we are in the process of examining RDX adsorption in several IRMOFs.

In this work, we report on our evaluation of IRMOF-10. The crystal structure of IRMOF-10 from the X-ray diffraction (XRD) data was given by Eddaoudi et al.⁶ as shown in Figure 2. IRMOF-10 maintains the cubic topology of the framework of the parent structure (IRMOF-1) but substitutes the connecting 1,4-benzenedicarboxylic acid (BDC) linker with a 4,4'-biphenyldicarboxylic acid (4,4'-BPDC). As a consequence, the structure of IRMOF-10 is similar to that of IRMOF-1 but is significantly

*To whom correspondence should be addressed. E-mail: dkeffer@utk.edu.

(1) Dionne, B. C.; Rounbehler, D. P.; Achter, E. K.; Hobbs, J. R.; Fine, D. H. *J. Energ. Mater.* **1986**, *4*, 447–472.

(2) Voiculescu, I.; et al. *IEEE Sens. J.* **2006**, *6*, 1094–1104.

(3) Senesac, L.; Thundat, T. G. *Mater. Today* **2008**, *11*, 28–36.

(4) Yaghi, O. M.; Li, G. M.; Li, H. L. *Nature* **1995**, *378*, 703–706.

(5) Li, H.; Eddaoudi, M.; O'Keeffe, M.; Yaghi, O. M. *Nature* **1999**, *402*, 276–279.

(6) Eddaoudi, M.; Kim, J.; Rosi, N.; Vodak, D.; Wachter, J.; O'Keeffe, M.; Yaghi, O. M. *Science* **2002**, *295*, 469–472.

(7) Duren, T.; Snurr, R. Q. *J. Phys. Chem. B* **2004**, *108*, 15703–15708.

(8) Rosi, N. L.; Eckert, J.; Eddaoudi, M.; Vodak, D. T.; Kim, J.; O'Keeffe, M.; Yaghi, O. M. *Science* **2003**, *300*, 1127–1129.

(9) Collins, D. J.; Zhou, H. C. *J. Mater. Chem.* **2007**, *17*, 3154–3160.

(10) Rowsell, J. L. C.; Millward, A. R.; Park, K. S.; Yaghi, O. M. *J. Am. Chem. Soc.* **2004**, *126*, 5666–5667.

(11) Fuentes-Cabrera, M.; Nicholson, D. M.; Sumpter, B. G.; Widom, M. *J. Chem. Phys.* **2005**, *123*, 124713.

(12) Ni, Z.; Jerrell, J. P.; Cadwallader, K. R.; Masel, R. I. *Anal. Chem.* **2007**, *79*, 1290–1293.

(13) Xiong, R.; Fern, J. T.; Keffer, D. J.; Fuentes-Cabrera, M.; Nicholson, D. M. *Mol. Simul.* **2009**, *35*, 910–919.

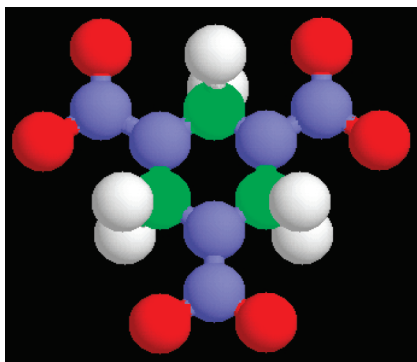


Figure 1. RDX structure (legend: N, blue; C, green; O, red; H, white).

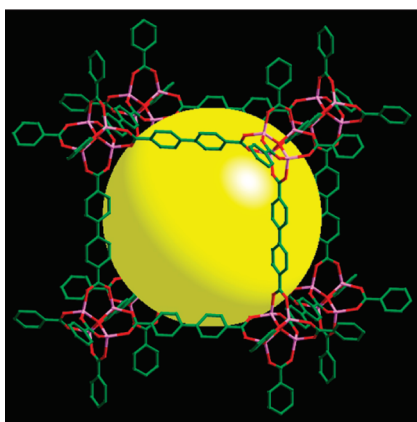


Figure 2. IRMOF-10 unit cell structure (legend: Zn, violet; C, green; O, red). All hydrogen atoms are not shown. The yellow sphere is located within the small cage.

larger. The unit cell length for IRMOF-1 is 25.832 Å, and the unit cell length for IRMOF-10 is 34.2807 Å.³ Like IRMOF-1, IRMOF-10 consists of two different kinds of alternating cages, denoted as big cage and small cage in our previous work,¹³ which reflects the orientation of the benzene rings as shown in Figure 2.

In order to use classical molecular simulations to examine the ability of IRMOF-10 to adsorb RDX, a model of the charge distribution in both IRMOF-10 and RDX is essential as an input to the simulation. There are several reports that evaluate the charge distribution for IRMOF-1, such as the MM3-based force field^{14,15} and the CVFF-based force field.^{16,17} In each of these cases, the classical distribution of charge is assumed to be point charges located at each atom center. Moreover, the magnitude of the charges is fixed in time. The MM3 force field,¹⁴ which is a fully bonded and flexible force field, along with the charge distribution, predicts the IRMOF-1 structure successfully. However, there is less information available for the charge distribution in IRMOF-10. Babarao and Jiang¹⁸ reported a set of IRMOF-10 atomic charges that are estimated from an electrostatic potential (ESP) using a B3LYP density functional theory (DFT) calculation. ESP is just one of the commonly used methods to estimate atomic

charges. Kawakami et al.¹⁹ have shown the loadings of CO₂ in a MOF crystal were affected by the charge densities calculated from different density functional methods. Moreover, the inclusion of charges on the framework atoms has been shown to shift the adsorption isotherms but not change the qualitative adsorption behavior for several adsorbate molecules, such as hydrogen²⁰ and benzene.²¹ A recent review²² points out the atomic charges of IRMOF-1 assigned using quantum mechanical (QM) calculations vary using different charge calculation methods, which may have a significant impact on the outcome of classical force field calculations in examples where electrostatic interactions are important.

In this work, we examine the effect of different charge distributions on the binding energies and adsorption isotherms of RDX in IRMOF-10. In each case, we limit ourselves to the same model for charge distributions that were used in IRMOF-1, namely that we place point charges on the atom centers and hold the values of these point charges fixed. We evaluate different charge distributions by comparing the binding energies from the classical potential with those from the QM calculations. Our goal is to determine the best choice of methods which should be used to generate charge distributions yielding the optimal computational results for the IRMOF-10 system. The criteria used for determining the best method could in general include comparing binding energies, adsorption isotherms, or self-diffusivities from simulation with experimental data. Unfortunately, for the case of RDX, there is no such experimental data available. Therefore, we use the QM calculations as the standard. (We accept that there is uncertainty associated with this standard.) The QM calculations provide binding energies but do not provide isotherms or diffusivities. Therefore, the criterion used to evaluate the goodness of the various charge distributions will be comparison with binding energies obtained from QM.

This work is focused on the electrostatic contribution as the source of greatest uncertainty in the description of the adsorbate–framework interactions in nanoporous materials. We are motivated by findings in the literature, which indicate polar molecules are more difficult to correctly simulate than nonpolar molecules. For example, the study of the adsorption of nonpolar molecules (such as hydrogen and methane) in MOFs, where the electrostatic are neglected and the Lennard-Jones (L-J) contributions represents 100% of the interaction, experimental isotherms can be reproduced well without adjustment to the interaction parameters.^{20,23} Moreover, for methane it has been shown that the isotherm is relatively insensitive to L-J parameters.²³ Furthermore, for polar molecules (like water), experimental adsorption isotherms in nanoporous materials can be reproduced by manipulation of the partial charges of the adsorbent framework.²⁴ Taken collectively, these findings point to the uncertainty in the charge distribution as a principal source of error.

2. Computational Details

2a. Quantum Mechanical Calculations. It is quite common in classical simulations to use interactions that are parametrized by point charges associated with atomic positions. The QM

(14) Tafipolsky, M.; Amirjalayer, S.; Schmid, R. *J. Comput. Chem.* **2007**, *28*, 1169–1176.

(15) Amirjalayer, S.; Tafipolsky, M.; Schmid, R. *Angew. Chem., Int. Ed.* **2007**, *46*, 463–466.

(16) Greathouse, J. A.; Allendorf, M. D. *J. Am. Chem. Soc.* **2006**, *128*, 10678–10679.

(17) Greathouse, J. A.; Allendorf, M. D. *J. Phys. Chem. C* **2008**, *112*, 5795–5802.

(18) Babarao, R.; Jiang, J. W. *Langmuir* **2008**, *24*, 6270–6278.

(19) Kawakami, T.; Takamizawa, S.; Kitagawa, Y.; Maruta, T.; Mori, W.; Yamaguchi, K. *Polyhedron* **2001**, *20*, 1197–1206.

(20) Garberoglio, G.; Skoulidas, A. I.; Johnson, J. K. *J. Phys. Chem. B* **2005**, *109*, 13094–13103.

(21) Sarkisov, L.; Duren, T.; Snurr, R. Q. *Mol. Phys.* **2004**, *102*, 211–221.

(22) Keskin, S.; Liu, J.; Rankin, R. B.; Johnson, J. K.; Sholl, D. S. *Ind. Eng. Chem. Res.* **2009**, *48*, 2355–2371.

(23) Duren, T.; Sarkisov, L.; Yaghi, O. M.; Snurr, R. Q. *Langmuir* **2004**, *20*, 2683–2689.

(24) Castillo, J. M.; Vlucht, T. J. H.; Calero, S. *J. Phys. Chem. C* **2008**, *112*, 15934–15939.

calculations were found to be useful in defining point charges on MOFs.²² There is no unique solution for mapping an electron distribution onto point charges which are assigned to atomic centers. Thus, to determine a charge distribution which is most appropriate to IRMOF-10, we evaluated different approaches for assigning charges—the ESP method²⁵ and three common non-ESP methods including Mulliken population analysis (MPA),^{26,27} Löwdin population analysis (LPA),²⁸ and the natural bond orbital (NBO)^{29,30} method. ESP,^{14,18,31} MPA,^{31,32} and NBO³² methods were used recently to study the charge population analysis of MOFs.

In the ESP method, atomic charges are fit to the molecular electrostatic potential, which is a rigorously defined QM property. The molecular electrostatic potential is calculated with the atomic wave function basis set. In the three non-ESP methods, atomic charges are determined by partitioning the electron density into atomic contributions. The weaknesses of both ESP and non-ESP methods are well-known. It has been shown by Sigfridsson and Ryde³³ that the atomic charges computed by the ESP method strongly depend on how and where the electrostatic potential points are selected. The non-ESP methods are very sensitive to the choice of basis set.^{34,35} Although the ESP method has proved to be more accurate in the description of intermolecular properties, the non-ESP charges remain interesting to show the variation in adsorption and diffusion when different charges are used.

We have used two ESP charge sets in this work. One of the ESP methods has previously been applied to IRMOF-10 by Babarao and Jiang.¹⁸ They have fit the electrostatic potential at grid points located with equal density on different layers around the molecule. In this work, their calculated charges are indicated as ESP-1.

In the second ESP method, the effective atomic charges in the MM3 force field for IRMOF-1 determined by Tafipolsky et al.¹⁴ were calculated by fitting to the electrostatic potential at a large number of points on or near the van der Waals surface. We extend this charge distribution to IRMOF-10 since the structure of IRMOF-10 is similar to that of IRMOF-1. For the atoms common to both IRMOF-1 and IRMOF-10 (Zn, O1, O2, C1, C2, C3, and H3; Figure 3a) we assigned the same charges to IRMOF-10 that were generated for IRMOF-1.¹⁴ As was done for Babarao and Jiang, the charges of the atoms C4 and H4 are, based on symmetry, set equal to the atoms C3 and H3, respectively. The charge of the remaining atom (C5) is adjusted to satisfy charge neutrality of the unit cell. All 10 independent atoms (Zn, O1, O2, C1, C2, C3, C4, C5, H3, and H4) of IRMOF-10 are indicated in Figure 3a. In this work, this set of charges extended from the MM3 force field is also employed. In order to differentiate the previous ESP charge set, we denote it as ESP-2.

For the MPA and NBO analyses, three cluster models are employed in this calculation, which are shown in Figure 3. Final charges are the average values of all symmetrical atoms from all three configurations. The MPA and NBO analyses are also performed at the DFT level^{36,37} as implemented in the Gaussian03 program package.³⁸ The hybrid Becke's three parameter with

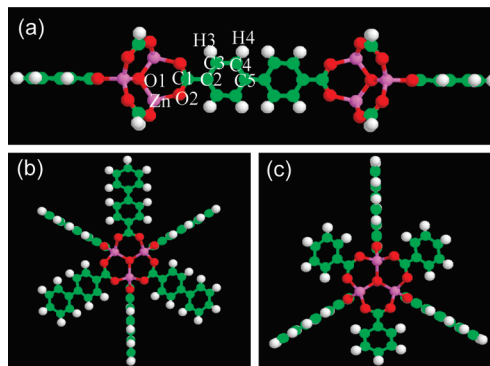


Figure 3. Three representative cluster models for calculating charge distribution in IRMOF-10 (legend: Zn, violet; C, green; O, red; H, white).

Lee–Yang–Parr correlation term (B3LYP) functional^{39,40} is used. B3LYP functional was chosen in the first place because it was successfully used in several other theoretical studies of MOFs^{14,41–43} and systems containing zinc complexes.⁴⁴ The LANL2DZ basis set,^{45,46} which uses an effective core potential on all metal atoms of IRMOF-10, is applied since this basis set is generally considered more appropriate for transition metal chemistry.

The LPA analysis are performed using the FIREBALL code,⁴⁷ which uses atomic orbitals to express electronic wave functions with finite cutoff lengths. The entire unit cell (as shown in Figure 2) of IRMOF-10 is used in the LPA analysis with periodic boundary conditions applied. Details of the methodology can be found elsewhere.^{48,49}

In addition to partial charges for IRMOF-10, we also vary the partial charges for RDX. One of the partial charge distributions for RDX are taken from Boyd et al.⁵⁰ The partial charges were calculated for crystalline RDX by fitting to a set of experimentally determined crystal properties. We also calculate charge distributions for ideal gas RDX and RDX in IRMOF-10 from QM calculations using ESP, MPA, NBO, and LPA. These ESP charges are obtained at points selected according to the Merz–Singh–Kollman scheme.^{51,52}

We should note that in this work we have varied the method that generates the charges from the QM electron distribution. The choice of level of theory and basis set also impacts the QM results that are inputs into the charge generation procedure and therefore indirectly affects the charges as well.

In order to evaluate the charge distributions used in the classical simulations, we compare the binding energy for a given configuration from the classical potential with that from the QM calculations. The QM binding energies are calculated as the relaxed energies (energy calculated after RDX is optimized) of the RDX/IRMOF-10 configurations less the relaxed energies of the isolated RDX molecule and IRMOF-10 cluster model.

(25) Cox, S. R.; Williams, D. E. *J. Comput. Chem.* **1981**, *2*, 304–323.

(26) Mulliken, R. S. *J. Chem. Phys.* **1955**, *23*, 1833–1840.

(27) Csizmadia, I. G. *Theory and Practice of MO Calculations on Organic Molecules*; Elsevier: Amsterdam, 1976.

(28) Löwdin, P. O. *J. Chem. Phys.* **1950**, *18*, 365–375.

(29) Foster, J. P.; Weinhold, F. *J. Am. Chem. Soc.* **1980**, *102*, 7211–7218.

(30) Reed, A. E.; Curtiss, L. A.; Weinhold, F. *Chem. Rev.* **1988**, *88*, 899–926.

(31) Tafipolsky, M.; Amirjalayer, S.; Schmid, R. *Microporous Mesoporous Mater.* **2010**, *129*, 304–318.

(32) Klontzas, E.; Mavrandonakis, A.; Tylanakakis, E.; Froudakis, G. E. *Nano Lett.* **2008**, *8*, 1572–1576.

(33) Sigfridsson, E.; Ryde, U. *J. Comput. Chem.* **1998**, *19*, 377–395.

(34) Reed, A. E.; Weinstock, R. B.; Weinhold, F. *J. Chem. Phys.* **1985**, *83*, 735–746.

(35) Mayer, I. *Chem. Phys. Lett.* **2004**, *393*, 209–212.

(36) Parr, R. G.; Yang, W. *Density-Functional Theory of Atoms and Molecules*; Oxford University Press: Oxford, 1989.

(37) Kohn, W.; Sham, L. J. *Phys. Rev.* **1965**, *140*, 1133–1138.

(38) Frisch, M. J. et al. *Gaussian 03, Revision C.02*; Gaussian, Inc.: Wallingford, CT, 2004.

(39) Becke, A. D. *J. Chem. Phys.* **1993**, *98*, 5648–5652.

(40) Lee, C. T.; Yang, W. T.; Parr, R. G. *Phys. Rev. B* **1988**, *37*, 785–789.

(41) Civalleri, B.; Napoli, F.; Noel, Y.; Roetti, C.; Dovesi, R. *CrystEngComm* **2006**, *8*, 364–371.

(42) Choomwattana, S.; Maihom, T.; Khongpracha, P.; Probst, M.; Limtrakul, J. *J. Phys. Chem. C* **2008**, *112*, 10855–10861.

(43) Yang, Q. Y.; Zhong, C. L. *J. Phys. Chem. B* **2006**, *110*, 655–658.

(44) Rotzinger, F. P. *J. Phys. Chem. B* **2005**, *109*, 1510–1527.

(45) Dunning, T. H., Jr.; Hay, P. J. In *Modern Theoretical Chemistry*; Plenum: New York, 1976.

(46) Hay, P. J.; Wadt, W. R. *J. Chem. Phys.* **1985**, *82*, 270–283.

(47) Lewis, J. P.; Glaesemann, K. R.; Voth, G. A.; Fritsch, J.; Demkov, A. A.; Ortega, J.; Sankey, O. F. *Phys. Rev. B* **2001**, *64*, 195103.

(48) Sankey, O. F.; Niklewski, D. J. *Phys. Rev. B* **1989**, *40*, 3979–3995.

(49) Sankey, O. F.; Demkov, A. A.; Windl, W.; Fritsch, J. H.; Lewis, J. P.; Fuentes-Cabrera, M. *Int. J. Quantum Chem.* **1998**, *69*, 327–340.

(50) Boyd, S.; Gravelle, M.; Politzer, P. *J. Chem. Phys.* **2006**, *124*, 104508.

(51) Besler, B. H.; Merz, K. M.; Kollman, P. A. *J. Comput. Chem.* **1990**, *11*, 431–439.

(52) Singh, U. C.; Kollman, P. A. *J. Comput. Chem.* **1984**, *5*, 129–145.

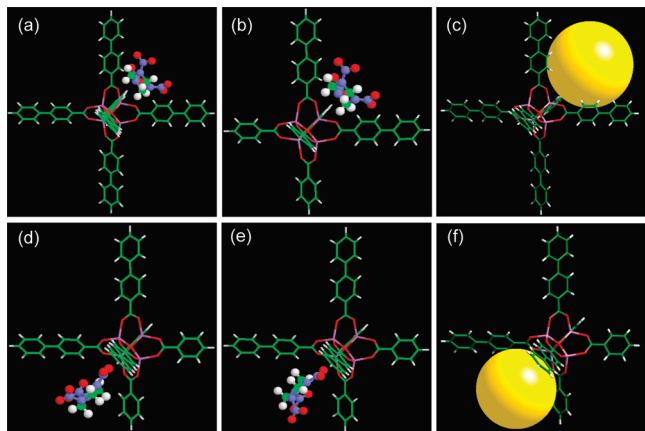


Figure 4. Four configurations of RDX in IRMOF-10 for which binding energies were calculated (legend: Zn, violet; N, blue; C, green; O, red; H, white): (a) SG = small cage, global minimum; (b) SL = small cage, local minimum; (c) a sphere indicating where RDX is located within the small cage; (d) BG = big cage, global minimum; (e) BL = big cage, local minimum; (f) a sphere indicating where RDX is located within the big cage.

Dangling bonds of the IRMOF-10 fragments are saturated by hydrogen atoms. The geometry of RDX is fully optimized while the geometry of the IRMOF-10 fragment is kept frozen (the full optimization leads to a slight change of the crystal structure of IRMOF-10, elongation of distances, and modification of bond and dihedral angles). The representative cluster models of IRMOF-10 are prepared as cutoffs from the crystal structure of IRMOF-10.⁶ Several different initial orientations of an RDX molecule and different sizes of IRMOF-10 fragments are tested in order to estimate the influence of the IRMOF-10 fragment on the binding energies and the intermolecular interactions. Ultimately, we report binding energies for four configurations corresponding to global and local minima in the big and small cages, as shown in Figure 4.

The interaction energy calculations were performed using the B3LYP-D functional⁵³ as implemented in the TURBOMOLE program package^{54,55} to include the dispersion correction into the intermolecular interactions because this type of correction is missing in regular B3LYP calculations. B3LYP-D includes a dispersion contribution with an empirical correction ($-C_6/R^6$) to the B3LYP functional. It has been shown that B3LYP-D provides significant improvements comparing B3LYP.^{56,57} The B3LYP-D functional was shown to have excellent performance in the study of H/Br exchange in BBr₃ by HSiR₃.⁵⁸ In addition, the B3LYP-D method was also shown in an excellent agreement with experimental data for structures and cohesive energies of a representative set of molecular crystals⁵⁹ as well as for anisole: ammonia 1:1 molecular complexes.⁶⁰

Additional calculations using B3LYP were performed to compare with B3LYP-D so that the discrimination between electrostatic and dispersive interactions in the QM calculations could be analyzed. Moreover, we have calculated the interaction energy using the B97-D functional, which also includes an empirical dispersion function and was suggested as an accurate QM method

for large systems where electrostatic interactions are important.⁶¹ However, B97-D is a reparameterization of the original Becke's hybrid-GGA functional, which includes a change in the exchange-correlation functional;⁶¹ thus, it is not just adding the dispersion correction. From comparing B3LYP-D with B97-D, one can understand the whole picture about the electrostatic and dispersion interactions.

The interaction energy (E_{int}) values are corrected by the basis set superposition error (BSSE) using the counterpoise method.⁶² The BSSE energy values are denoted as E_{bsse} , and the interaction energy values after the BSSE correction are denoted as E_{corr} .

2b. Classical Simulations. We perform GCMC simulations to calculate the adsorption properties and MD simulations to calculate the diffusivities for RDX in IRMOF-10. We have previously reported classical simulations (both MD and GCMC simulations) of RDX in IRMOF-1.¹³ The simulations in this work use the same procedure and potentials, except, in this work, the charge distributions within IRMOF-10 and RDX are varied. We use a rigid structure to model IRMOF-10 in our simulations. The atomic positions of the structure are obtained from published X-ray diffraction data.⁶ The RDX potential is fully flexible. RDX molecules interact with each other and with the atoms of the IRMOF-10 framework through a combination of L-J 12–6 potential and Coulombic interactions. The Coulombic interactions are handled by the spherically truncated charge-neutralized procedure of Wolf et al.⁶³ The RDX–RDX and RDX–IRMOF-10 intermolecular L-J interaction potentials are truncated at 18 Å. Periodic boundary conditions are applied.

In both GCMC and MD simulations, the temperature is 300 K, and an average of ~1000 molecules are maintained in each simulation to obtain good statistics. The GCMC simulations are performed at the ideal gas bulk pressure ($\sim 9.4 \times 10^{-7}$ bar) and consist of a total of at least 3×10^8 trial moves, the last one-third of which are used for data production. Four types of trial moves (translation, rotation, insertion, and deletion) are involved, the ratios of which are 4:2:3:3, respectively. The MD simulations are performed with the average loading of RDX in IRMOF-10 at 300 K and $\sim 9.4 \times 10^{-7}$ bar. The MD simulations are allowed to equilibrate for 2 ns, and subsequently mean-square displacement (MSD) data are collected for 20 ns. More detailed information is available in the previous work.¹³

3. Results and Discussion

In this section, we present charges, binding energies, points on the RDX adsorption isotherm, and RDX self-diffusivities as a function of charge set. To clarify the relative performance of different charge distributions, we study 15 different choices for the charges. The 15 combinations are summarized in Table 1. Each set of charges are obtained with a particular method for a particular configuration. For example, the states for RDX include the crystal phase, the ideal gas phase, and the adsorbed phase within IRMOF-10. The states for IRMOF-10 include the case when the pore is empty and the case when the pore contains one RDX molecule (averaged over four positions for the adsorbed RDX). We shall further discuss the various choice of methods used to generate charge distributions below. The first five combinations focus on the variation of atomic charges on IRMOF-10 while fixing the atomic charges of RDX from a fit to experimental data. The next 10 combinations focus on systematic variation of the atomic charges of both RDX and IRMOF-10. While there are other possible combinations, the 15 chosen span the interesting parameter space.

(53) Grimme, S. *J. Comput. Chem.* **2004**, *25*, 1463–1473.

(54) Ahlrichs, R. *TURBOMOLE* (v. 5.6); Universität Karlsruhe, 2003.

(55) Ahlrichs, R.; Bar, M.; Haser, M.; Horn, H.; Kolmel, C. *Chem. Phys. Lett.* **1989**, *162*, 165–169.

(56) Schwabe, T.; Grimme, S. *Phys. Chem. Chem. Phys.* **2007**, *9*, 3397–3406.

(57) Uglierio, P.; Zicovich-Wilson, C. M.; Tosoni, S.; Civalleri, B. *J. Mater. Chem.* **2009**, *19*, 2564–2572.

(58) Rakow, J. R.; Tullmann, S.; Holthausen, M. C. *J. Phys. Chem. A* **2009**, *113*, 12035–12043.

(59) Civalleri, B.; Zicovich-Wilson, C. M.; Valenzano, L.; Uglierio, P. *CrysEngComm* **2008**, *10*, 405–410.

(60) Barone, V.; Biczysko, M.; Pavone, M. *Chem. Phys.* **2008**, *346*, 247–256.

(61) Grimme, S. *J. Comput. Chem.* **2006**, *27*, 1787–1799.

(62) Boys, S. F.; Bernardi, F. *Mol. Phys.* **1970**, *19*, 553–566.

(63) Wolf, D.; Keblinski, P.; Phillpot, S. R.; Eggebrecht, J. *J. Chem. Phys.* **1999**, *110*, 8254–8282.

Table 1. Different Combinations Used To Generate Sets of Charges for the Classical GCMC and MD Simulations

run id	RDX state	RDX method	MOF state	MOF method
1	crystal	ref 50	empty	ESP-1
2	crystal	ref 50	empty	ESP-2
3	crystal	ref 50	empty	NBO
4	crystal	ref 50	empty	MPA
5	crystal	ref 50	empty	LPA
6	ideal gas	NBO	empty	ESP-1
7	ideal gas	LPA	empty	ESP-1
8	ideal gas	NBO	empty	ESP-2
9	ideal gas	LPA	empty	ESP-2
10	ideal gas	NBO	empty	NBO
11	ideal gas	MPA	empty	MPA
12	ideal gas	LPA	empty	LPA
13	adsorbate	NBO	w/RDX	NBO
14	adsorbate	MPA	w/RDX	MPA
15	adsorbate	LPA	w/RDX	LPA

Table 2. Charge Distributions for Atoms of IRMOF-10 Based on an Empty Cage

atom	MPA	LPA	NBO	ESP-1	ESP-2
Zn	1.083	0.788	1.392	1.420	1.260
O1	−1.170	−0.509	−1.443	−1.680	−1.440
O2	−0.501	−0.255	−0.795	−0.710	−0.670
C1	0.290	0.136	0.868	0.720	0.680
C2	0.232	−0.120	−0.150	0.130	0.060
C3	−0.388	−0.082	−0.113	−0.210	−0.160
C4	−0.433	−0.081	−0.165	−0.210	−0.160
C5	0.371	−0.032	−0.024	0.130	0.000
H3	0.329	0.102	0.202	0.150	0.160
H4	0.283	0.104	0.179	0.150	0.160

In Table 2, we show the charge distribution of IRMOF-10 from the MPA, LPA, NBO, and ESP applied to the empty cage. For all of the atoms involved in the octahedral zinc carboxylate complex (Zn, O1, O2, and C1 of Figure 3a) the five sets of charges provide the same sign of the charge for each atom, although the magnitude varies significantly. For the atoms in the Zn carboxylate complex, LPA generally gives the smallest partial charges, while NBO and ESP-1 give the largest partial charges. For the atoms involved in the benzene ring (C2, C3, C4, C5, H3, and H4), the LPA, NBO, ESP-1, and ESP-2 charges are in generally good agreement, with charges that are an order of magnitude smaller than the charges of the atoms in the metal complex. The exception is MPA, which gives significantly larger negative charges to the carbon and larger positive charges to the hydrogen of the benzene rings.

We can understand the differences in charges as a function of the method in part by understanding the approximations that go into the charge-generating procedures. In general, LPA provides the smallest partial charges, which is a consequence of the limited number of atomic orbitals used in LPA. It has been previously found that LPA charges are smaller in magnitude than MPA charges,^{64–66} which is an observation of the differences between the two methods, rather than a judgment of their relative merits. MPA tends to overestimate the covalent character of a bond (underestimating the bond ionicity and the degree of charge separation between electropositive and electronegative atoms).⁶⁷ Consequently, electropositive atoms like C3 and C4 have larger negative partial charges in MPA than they do, for example, with NBO. At the same time, electronegative atoms like O1 and O2

Table 3. Charge Distributions for Atoms on IRMOF-10 with One RDX in the Cage

atom	MPA	LPA	NBO
Zn	1.069	0.795	1.720
O1	−1.173	−0.513	−1.715
O2	−0.507	−0.257	−0.875
C1	0.308	0.139	0.870
C2	0.229	−0.122	−0.165
C3	−0.384	−0.083	−0.115
C4	−0.423	−0.081	−0.170
C5	0.376	−0.031	−0.022
H3	0.323	0.102	0.204
H4	0.276	0.103	0.183

have smaller negative charges in MPA than in NBO. The NBO analysis, in contrast, predicts a much more positive charge on electropositive atoms. This explains the difference between the charges on oxygens and carbons when comparing the results of NBO and MPA analyses. This fact also causes the charge on C5 to change sign from positive with MPA to negative with NBO.

In Table 3, we show the MPA, LPA, and NBO charge sets for IRMOF-10 obtained when one RDX molecule is adsorbed in the cage. These charges are averaged over the four configurations in Figure 4. In these configurations, the charges vary by about 2% from one configuration to another. The relative change in average charge on the MOF due to the presence of RDX is 1.9% for MPA, 1.2% for LPA, and 7.9% for NBO. The NBO charges of Zn and O1 have a significant change in the presence of RDX. All other changes are relatively small. The differences between the partial charges obtained from MPA, LPA, and NBO are due to the same reasons as given above for Table 2.

In Table 4, we compare the charges calculated for RDX. We include atomic charges from experimental fitting of mechanical properties of crystalline RDX.⁵⁰ We also include the DFT calculations for RDX in the ideal gas and RDX adsorbed in IRMOF-10. Even in the ideal gas, there is a great discrepancy between charges from the four methods, MPA, LPA, NBO, and ESP. As was the case in IRMOF-10, MPA gives a much larger charge separation to the C and H atoms. The NBO and ESP methods give a large charge separation to the N and O atoms of the nitro group. The ESP method also gives significant charge separation to the C and N of the ring, not seen in any of the other models. A comparison of charges for RDX in the ideal gas and adsorbed phase shows a relative change in average charge of 33% for MPA, 11% for LPA, 6% for NBO, and 158% for ESP.

One method of evaluating the various charge sets is to compare the binding energy from the classical potentials with the QM binding energy for the four configurations shown in Figure 4. These four configurations of RDX in IRMOF-10 correspond to a global-minimum QM energy structure (the lowest energy found via QM in this work) with RDX in the small cage (SG = small, global; Figure 4a), a local-minimum energy structure with RDX in the small cage (SL = small, local; Figure 4b), a global-minimum energy structure with RDX in the big cage (BG = big, global; Figure 4d), and a local-minimum energy structure with RDX in the big cage (BL = big, local; Figure 4e). The additional two structures that contain the yellow spheres are included to help visualize the volume where the RDX is located in the small (Figure 4c) and big cages (Figure 4f).

The QM binding energies of these four configurations are reported in Table 5. The weakest binding is obtained with B3LYP functional whereas the dispersion-corrected B3LYP-D functional leads to much larger bindings. Despite such differences in the energy, the general trend regarding the stability of RDX on different IRMOF-10 fragment remains the same. E_{bsse} is much

(64) Kar, T.; Sannigrahi, A. B. *THEOCHEM* **1988**, *42*, 47–54.(65) Segall, M. D.; Pickard, C. J.; Shah, R.; Payne, M. C. *Mol. Phys.* **1996**, *89*, 571–577.(66) Chojnacki, H. *Int. J. Mol. Sci.* **2003**, *4*, 481–485.(67) Martin, F.; Zipse, H. *J. Comput. Chem.* **2005**, *26*, 97–105.

Table 4. Charge Distributions for Atoms on RDX

atom	crystal	ideal gas				adsorbate			
		MPA	LPA	NBO	ESP	MPA	LPA	NBO	ESP
C	0.057 52	−0.266 10	0.059 21	−0.048 50	−0.219 54	−0.336 11	0.037 54	−0.049 78	−0.695 71
N	−0.137 20	−0.066 73	−0.182 98	−0.288 47	0.061 78	−0.042 10	−0.192 03	−0.329 49	0.350 54
N (nitro)	0.271 57	0.132 63	0.174 11	0.618 97	0.735 75	0.209 35	0.178 35	0.604 58	0.663 07
O	−0.267 24	−0.199 64	−0.130 56	−0.404 09	−0.452 81	−0.223 27	−0.123 18	−0.387 69	−0.429 41
H	0.100 81	0.299 74	0.105 39	0.263 09	0.163 82	0.310 29	0.112 89	0.275 66	0.309 47

Table 5. BSSE-Corrected Interaction Energies (kcal/mol) of RDX Interacting with IRMOF-10 Fragments Calculated at the B3LYP, B3LYP-D, and B97-D Levels of Theory

system	SG			SL			BG			BL		
	B3LYP	B97-D	B3LYP-D	B3LYP	B97-D	B3LYP-D	B3LYP	B97-D	B3LYP-D	B3LYP	B97-D	B3LYP-D
E_{int}	−12.6	−27.6	−30.7	−14.5	−27.4	−30.4	−7.8	−16.8	−18.8	−5.1	−16.4	−18.5
E_{bsse}	4.5	4.6	8.2	7.8	4.6	8.1	3.6	4.4	7.0	4.5	4.4	6.9
E_{corr}	−8.1	−23.0	−22.5	−6.7	−22.8	−22.3	−4.2	−12.4	−11.8	−0.6	−12.0	−11.6

more pronounced at the B3LYP level, ranging from 3.6 kcal/mol (BG) to 7.8 kcal/mol (SL), which accounts for 47% and 54% of E_{int} , and stems mainly from the contribution of the IRMOF-10 fragment. The most significant finding is that noncovalent (dispersion) interactions appear to be a very important contributor to the total binding energy. This is apparent from the B3LYP and B3LYP-D comparison, which suggests that dispersion interactions involving a single RDX molecule interacting with the small cage site of IRMOF-10 can sum up from 14 to 15 kcal/mol (about 64%–68% of E_{corr}). The same effect is observed for a configuration with weaker interaction (BG), where the RDX binding energy is −11.8 kcal/mol and the dispersion correction is −7.6 kcal/mol (about 64% of E_{corr}).

Comparison of the energies in Table 5 indicates that the dispersion term changes significantly when the RDX is in the small or big cages. The dispersion contribution is much larger than was found for the interaction energies of small strongly H-bonded complexes (about 10–30%).⁵³ On the other hand, almost the same trend for the interaction energy and dispersion contribution were found in the study of transition-metal triphenylphosphine complexes at the B3LYP and DFT-D levels of theory,⁶⁸ where the authors concluded that the dispersion contribution is large and gradually increases with the bulkiness of the ligand. Also in the study of Mg(OH)₂, Ca(OH)₂, and kaolinite,⁵⁷ the interlayer interaction energy increases largely due to the dispersion contribution obtained from comparison of the B3LYP and B3LYP-D results. The dispersion correction for anisole–ammonia 1:1 complex was also revealed to be quite large (about 40%),⁶⁰ and in the case of the benzene dimer the inclusion of the dispersion correction was found to be crucial because the bare B3LYP functional does not predict bound complexes, in contrast to the experimental observations.⁶⁹

For comparison, the B97-D calculation results of the interaction energies for all studied systems are also shown in Table 5. The resulting energy values from this calculation are only slightly larger than those found from the B3LYP-D, and also the BSSE values do not change significantly.

The energy analysis of data in Table 5 also reveals that the most strongly bound RDX molecules are those bound to the small cage structure. The most energetically favorable orientation of RDX (SG) is such that a C–H group of RDX is located at the midpoint between two oxygen atoms of the ZnO₄ fragment of the small

cage. The preferred binding to the big cage fragment (BG) occurs when RDX has an oxygen atom of one nitro group approaching the connector of the big cage fragment. A less stable structure (BL) is found to be the system containing the big cage and RDX oriented toward the cage by one N–O group and one C–H group. The binding energies of above-discussed configurations at B3LYP level are close to the values found in *ab initio* study of the adsorption of RDX on IRMOF-1.⁷⁰ RDX was revealed to interact more preferably with the 1,4-benzenedicarboxylate site (binding energy value amounts to about −9 kcal/mol) than with the [Zn₄O(CO₂)₆] site of IRMOF-1 (binding energy is about −5 kcal/mol).

In Table 6, the binding energies for the 15 different charge sets used in the classical GCMC simulations are reported. In the classical simulation, there are three contributions to the potential energy: intramolecular energy of the RDX (bond stretching, bending, torsion, etc.), intermolecular interactions between RDX and other RDX, and intermolecular interactions between RDX and the MOF. The binding energy is the difference in this potential energy between the adsorbed phase and the bulk phase. The intramolecular energy of RDX is the same in the bulk and adsorbed phase and cancels out of the binding energy. There is virtually no RDX–RDX interaction in the bulk phase and no RDX–MOF interaction, so the binding energy is essentially the RDX–RDX and RDX–MOF interactions in the adsorbed phase. Additionally, some key energy differences are reported. What is immediately apparent is that there is significant variation among the different point-charge sets and that none of them have quantitative agreement with the QM calculations. The differences are manifested in several ways.

First, the magnitudes of the binding energies are significantly different. The classical binding energies range from −0.99 to −16.86 kcal/mol, while the B3LYP binding energies are smaller, ranging from −0.60 to −8.10 kcal/mol, and the B3LYP-D binding energies are larger, ranging from −11.6 to −22.5 kcal/mol. Second, the energy changes between two configurations in the same cage, as captured by the change in binding energies, SG–SL and BG–BL, are different. From the B3LYP analysis there are relatively large changes in binding energy with small changes in configuration for small (−1.40 kcal/mol) and big (−3.60 kcal/mol) cages. From the B3LYP-D analysis, the relative changes in the binding energy, −0.20 (both small and big cage), are much

(68) Sieffert, N.; Buhl, M. *Inorg. Chem.* **2009**, *48*, 4622–4624.(69) Pavone, M.; Rega, N.; Barone, V. *Chem. Phys. Lett.* **2008**, *452*, 333–339.(70) Petrova, T.; Michalkova, A.; Leszczynski, J. *Struct. Chem.* **2009**, in press, doi: 10.1007/s11224-009-9542-9.

Table 6. Classical Single-Point Energies Compared with Quantum Binding Energies

model	corrected QM interaction energy (kcal/mol)			classical single-point energy (kcal/mol)							
	B3LYP	B97-D	B3LYP-D	1	2	3	4	5	6	7	8
BG	−4.20	−12.4	−11.8	−1.70	−2.46	−2.29	−0.99	−5.18	−4.53	−2.74	−4.13
BL	−0.60	−12.0	−11.6	−1.73	−2.50	−2.33	−1.06	−5.27	−4.61	−2.77	−4.21
SG	−8.10	−23.0	−22.5	−7.31	−10.41	−12.96	−13.82	−4.06	−12.27	−6.86	−13.29
SL	−6.70	−22.8	−22.3	−7.39	−10.51	−13.10	−13.98	−4.13	−12.38	−6.97	−13.45
SG-SL	−1.40	−0.20	−0.20	0.08	0.10	0.14	0.16	0.07	0.11	0.11	0.16
BG-BL	−3.60	−0.40	−0.20	0.03	0.04	0.04	0.07	0.09	0.08	0.03	0.08
SG-BG	−3.90	−10.6	−10.7	−5.61	−7.95	−10.67	−12.83	1.12	−7.74	−4.12	−9.16

model	corrected QM interaction energy (kcal/mol)			classical single-point energy (kcal/mol)						
	B3LYP	B97-D	B3LYP-D	9	10	11	12	13	14	15
BG	−4.20	−12.4	−11.8	−2.58	−5.14	−3.79	−3.83	−6.84	−3.43	−3.69
BL	−0.60	−12.0	−11.6	−2.62	−5.23	−3.83	−3.89	−6.96	−3.47	−3.75
SG	−8.10	−23.0	−22.5	−7.36	−16.66	−13.92	−2.62	−15.83	−13.86	−2.63
SL	−6.70	−22.8	−22.3	−7.50	−16.86	−14.21	−2.69	−16.07	−14.09	−2.70
SG-SL	−1.40	−0.20	−0.20	0.14	0.20	0.29	0.07	0.24	0.23	0.07
BG-BL	−3.60	−0.40	−0.20	0.04	0.09	0.04	0.06	0.12	0.04	0.06
SG-BG	−3.90	−10.6	−10.7	−4.78	−11.52	−10.13	1.21	−8.99	−10.43	1.06

Table 7. Potential Energies (kcal/mol) from GCMC Simulations at 300 K and $\sim 9.4 \times 10^{-7}$ bar

run id	RDX–RDX		RDX–IRMOF10		total potential (kcal/mol)		
	L-J	electrostatic	L-J	electrostatic	L-J	electrostatic	total (kcal/mol)
1	-9.93×10^{-8}	1.20×10^{-5}	−1.37	−8.88	−1.37	−8.88	−10.25
2	-3.58×10^{-8}	6.86×10^{-6}	−1.59	−7.22	−1.59	−7.22	−8.81
3	-1.31×10^{-6}	2.58×10^{-4}	−1.37	−10.67	−1.37	−10.67	−12.03
4	-2.64×10^{-5}	2.38×10^{-3}	−0.40	−11.60	−0.40	−11.59	−12.00
5	-3.76×10^{-3}	4.87×10^{-1}	−0.36	−18.57	−0.36	−18.08	−18.44
6	−1.62	−15.10	−0.53	−5.44	−2.15	−20.55	−22.71
7	-4.49×10^{-8}	-3.77×10^{-8}	−1.99	−3.49	−1.99	−3.49	−5.49
8	−1.45	−14.00	−0.56	−4.86	−2.01	−18.83	−20.84
9	-2.60×10^{-8}	3.83×10^{-8}	−1.81	−2.58	−1.81	−2.58	−4.39
10	−1.58	−13.70	−0.30	−7.32	−1.87	−20.98	−22.85
11	-4.24×10^{-2}	-3.85×10^{-1}	−1.01	−14.87	−1.06	−15.26	−16.31
12	-1.93×10^{-7}	-5.14×10^{-8}	−1.93	−6.94	−1.93	−6.94	−8.87
13	−1.67	−12.40	0.20	−10.26	−1.47	−22.68	−24.15
14	-2.70×10^{-2}	−0.21	−1.34	−13.77	−1.37	−13.97	−15.35
15	-1.93×10^{-7}	2.37×10^{-7}	−1.96	−6.23	−1.96	−6.23	−8.19

smaller. The classical charge sets result in less sensitivity to small changes in configuration leading to at most energy differences of 0.29 and 0.12 kcal/mol for the small and big cages, respectively. Third, the sign of the energy change from one configuration to another within the same cage is universally of the wrong sign for all classical potentials compared to either of the QM results. Fourth and finally, there is significant variation in the difference in binding energy between the big and small cages for the various classical charge sets, ranging from −12.83 to 1.21 kcal/mol. The difference in binding energy between the small and large cages (SG-BG) from the B3LYP calculations is −3.90 kcal/mol while the same difference for B3LYP-D is −10.7 kcal/mol due to the inclusion of the dispersion correction. In general, the LPA charge sets give closer agreement for this energy difference to the B3LYP results, and the NBO and MPA charge sets give closer agreement to the B3LYP-D results.

We next examine the impact of the choice of charge distribution on the adsorption of RDX in contributions to the energy as well as on the one-point adsorption isotherm at a temperature of 300 K and a bulk pressure of $\sim 9.4 \times 10^{-7}$ bar. This low pressure is relevant since we are interested in concentrating RDX from the gas phase in which the vapor pressure is very low. We have previously shown that for RDX in IRMOF-1 this bulk loading is in the relevant Henry's law regime of adsorption.¹³ In Table 7, we present the L-J and electrostatic contributions to the potential

energy due to RDX–RDX interactions, RDX–IRMOF-10 interactions, and the sum of the both interactions. Considering all but the NBO charge sets (set 6, 8, 10, and 13), the L-J contribution to the RDX–RDX interaction is at least 2 orders of magnitude smaller than the electrostatic contribution to the RDX–RDX interaction. However, the RDX–RDX electrostatic contribution is at least 2 orders of magnitude smaller than the RDX–IRMOF-10 electrostatic energy. That the RDX–RDX interactions are small is an indication of the fact that the adsorbate is present in low loadings. For the RDX–IRMOF-10 interactions, the fraction of the total energy that is due to the L-J contribution varies significantly, from 2% (set 5) to 41% (set 9), with an average of 14%. On the basis of the additional insight provided by the QM calculations above, we observe that the dispersion correction in the QM calculation results in a significant contribution to the total interaction energy, as much as 68%. However, the charge sets with large relative contributions from the L-J interaction have small contributions from the electrostatic interactions and are therefore in poor agreement with the B3LYP-D energies. This poor agreement demonstrates that the inability of this classical simulation to capture the total interaction energy between RDX and IRMOF-10 could at least in part be due to shortcomings of the L-J potential or its parameters in this application.

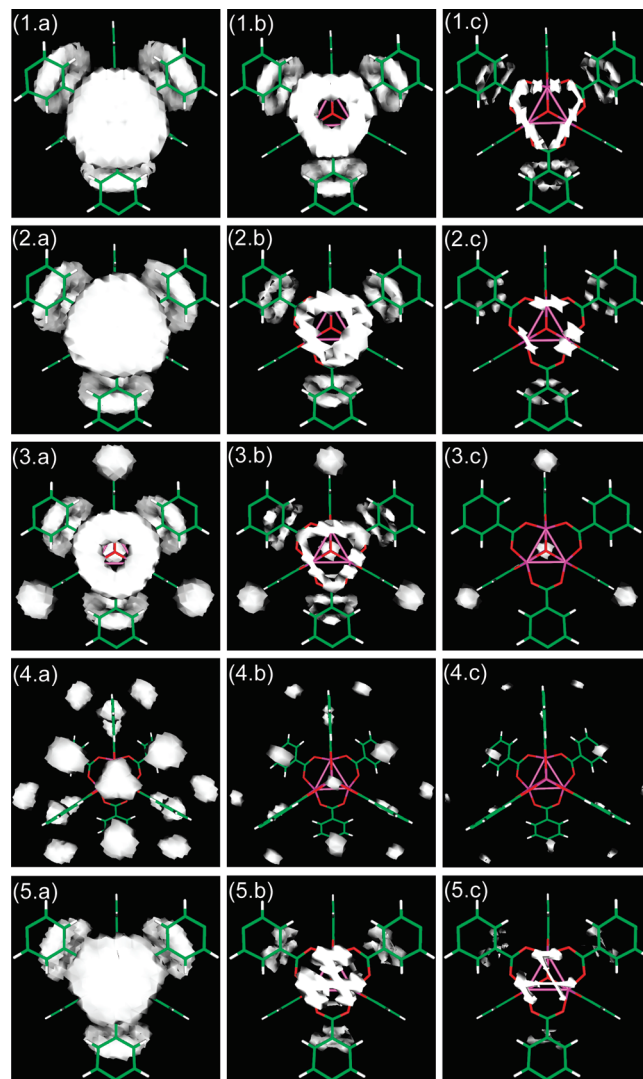
Table 8. Adsorption Loading and Self-Diffusivities at 300 K and $\sim 9.4 \times 10^{-7}$ bar

run id	adsorption loading (molecule/cage)	self-diffusivity (m^2/s)
1	3.41×10^{-5}	$1.52 \times 10^{-11} \pm 4.37 \times 10^{-12}$
2	2.67×10^{-5}	$8.36 \times 10^{-10} \pm 9.65 \times 10^{-11}$
3	5.02×10^{-4}	$1.71 \times 10^{-10} \pm 1.33 \times 10^{-11}$
4	5.48×10^{-3}	$2.86 \times 10^{-10} \pm 9.09 \times 10^{-12}$
5	4.92×10^{-1}	$1.28 \times 10^{-14} \pm 1.84 \times 10^{-15}$
6	condense (> 14)	$7.96 \times 10^{-13} \pm 2.23 \times 10^{-13}$
7	1.20×10^{-6}	$2.99 \times 10^{-9} \pm 1.86 \times 10^{-10}$
8	condense (> 14)	$1.26 \times 10^{-12} \pm 4.27 \times 10^{-13}$
9	8.37×10^{-7}	$4.46 \times 10^{-9} \pm 3.76 \times 10^{-11}$
10	condense (> 14)	$1.15 \times 10^{-12} \pm 1.17 \times 10^{-13}$
11	1.25×10^{-1}	$1.32 \times 10^{-11} \pm 1.04 \times 10^{-12}$
12	2.29×10^{-5}	$1.35 \times 10^{-10} \pm 1.52 \times 10^{-11}$
13	condense (> 14)	$1.21 \times 10^{-12} \pm 1.97 \times 10^{-13}$
14	6.44×10^{-2}	$2.16 \times 10^{-11} \pm 6.81 \times 10^{-14}$
15	1.17×10^{-5}	$2.26 \times 10^{-10} \pm 1.31 \times 10^{-11}$

We observe a different behavior for the charge sets that employed NBO. In those cases, the large positive charge on the N atom and correspondingly large negative charge on the O atoms of the RDX nitro group resulted in condensation of the RDX within the IRMOF-10 cage. In this case, the RDX–RDX interaction is actually larger than the RDX–IRMOF-10 interaction. At this point in time, it is unclear whether this condensation is physical. The system has a low bulk RDX pressure (about 10^{-6} bar) and a temperature of 300 K. There is insufficient experimental evidence to indicate whether condensation should occur within the nanopore at these conditions. Therefore, we cannot rule out the possibility that the NBO charge sets capture a real behavior.

The binding energy has a direct correlation to the amount of RDX that is adsorbed. In Table 8, we report the number of molecules of RDX adsorbed per cage. All GCMC simulations that used NBO charge sets resulted in condensation with at least 14 RDX molecules per cage. These NBO GCMC simulations had not completely finished equilibrating (there was a very slight rise in density still occurring, as one would expect due to the low probability of GCMC insertions in high density systems). The lowest adsorption energy for systems that do condense is -20.8 kcal/mol (system 8; NBO RDX and ESP-2 MOF). The highest adsorption energy for systems that do not condense is -18.4 kcal/mol (system 5; RDX from ref 50 and LPA MOF). Thus, we can establish a relatively small range between the two values at which condensation of RDX would likely occur. At the other extreme (system 9; LPA RDX and ESP-2 MOF) has the lowest binding energy and adsorbs the least amount of RDX (about 7 orders of magnitude less RDX than the condensed systems). For systems with intermediate adsorption energies, the relative amount of RDX adsorbs tracks very closely with the energy of adsorption.

There is also a challenge in reconciling the average total potential energy reported in Table 7 with the classical energies of the configurations reported in Table 6. The results from group 2, 3, 4, 7, and 9 are consistent with an intuitive understanding that the average energies from a simulation at 300 K have to be higher than the single-point energies reported in Table 6. These single-point energies correspond to configurations that were global and local minima in the QM calculations. It is at least qualitatively reasonable that the RDX molecules experience an average potential energy of -8.81 , -12.03 , -12.00 , -5.49 , and -4.39 kcal/mol at 300 K when the energy minimum is at -10.51 , -13.10 , -13.98 , -6.97 , and -7.50 kcal/mol for the group 2, 3, 4, 7, and 9. However, the energies in Tables 6 and 7 for other groups require further investigation.

**Figure 5.** Density distributions of RDX in IRMOF-10 for the first five combinations from vertex view at 300 K and infinite dilution. The density contour level is from low to high (legend: Zn, violet; C, green; O, red; H, white).

The average total potential energy of an RDX molecule in the GCMC simulation, as reported in Table 7, is lower than the energies associated with the configurations in Table 6, for the charge sets from group 1, 5, 11, 12, 14, and 15. The only way such a result is possible is if the configurations evaluated in Table 6 (which correspond to minima in the QM energy landscape) do not correspond to minima in the classical energy landscapes. We tested this hypothesis by randomly sampling RDX molecules from the GCMC simulations and performing single-point energy calculations. Indeed, our single-point energy calculations show that some configurations from the GCMC simulations provide deeper energies than the QM binding energy.

The difference between the QM and classical energies is not strictly in the depth of the well. From the GCMC simulations, we have generated density distributions, which are shown in Figure 5. In Figure 5, we have shown density distributions of the RDX center of mass in IRMOF-10 for the first five charge sets. The ESP-1, ESP-2, and LPA charge sets are qualitatively similar, placing the primary adsorption site of RDX in front of the cage vertex in the big cages. The NBO charge set has an adsorption site at the same location as ESP-1, ESP-2, and LPA but has a deeper adsorption site at the vertex of the small cages. This additional

adsorption site is presumably due to the very large charges placed on the nitro group by the NBO procedure. The MPA charge set has small adsorption sites at the vertex and deep adsorption sites in front of the benzene rings in the small cages. This difference in MPA is due to the large charge separation on the benzene rings using the MPA procedure.

It is also worth noting that in Table 7 the small cage had a deeper binding energy than the big cage for every charge set except sets 12 and 15. However, from the density distributions we observe preferential adsorption in the big cages for many of these charge sets. Of course, the preference of RDX for a big cage is a combination of energetic and entropic effects and cannot completely be explained by differences in 0 K binding energies. However, we do see deeper energetic wells in the big cage using the ESP-1 and ESP-2 charges than are evident in the optimized configurations from the QM calculations; i.e., the average energies of adsorption in Table 7 are greater in magnitude than the energies of the configurations reported in Table 6 that correspond to minima in the QM calculations. Therefore, the conclusion in the comparison of Tables 6 and 7 is that the configurations associated with minima in the QM energy landscape do not necessarily correspond to minima in the classical energy landscape. Therefore, there is no contradiction between the density distributions in Figure 5 and the energies in Table 6.

In Table 8, we also report the self-diffusivity of RDX from independent MD simulations run at the loadings generated from the GCMC simulations and reported in Table 8. There is a general correlation between the average energy of adsorption and the self-diffusivity, in which an increase in the magnitude of the energy of adsorption corresponds to a decrease in the self-diffusivity. This relationship is not unexpected since diffusion of RDX in MOFs is an activated process,¹³ and the activation energy is the difference in energy between the energy peak along the diffusion path (transition state energy) and the site energy. The energy of adsorption reported in Table 7 is an average over all energies and thus does not necessarily contain the activation energy. However, we do observe this general correlation, likely indicating that the change in charge set has a bigger impact on the adsorption site energy than on the diffusional transition state energy.

When examining the diffusivity as a function of density for a given potential, in general one expects that the diffusivity should decrease as the loading increases due to steric hindrances. However, we cannot make this correlation between the diffusivities and loadings in Table 8 because the potential is different for each case. Thus, the depths of the energy wells are different, which impact the activation energy for diffusion more so than does the loading.

4. Conclusions

Motivated to understand how RDX is absorbed in IRMOF-10 and how it diffuses within it, we perform classical GCMC and MD simulations of RDX in IRMOF-10. For this purpose force fields are evaluated by comparing binding energies obtained from them with the binding energies obtained from QM. We found that the choice of force field greatly affects the outcome.

We have shown that four different approaches for generating point charges of IRMOF-10 from QM calculations, including the electrostatic potential (ESP) method, Mulliken population analysis (MPA), Löwdin population analysis (LPA), and natural bond order (NBO) analysis, yield significantly different charges. Fifteen combinations are formed by applying different methods for charge calculation to different RDX/IRMOF-10 structures.

Comparison of the binding energies for fixed configurations of RDX in IRMOF-10 show great variation between the 15 combinations, none of which agree particularly well with the binding energy from quantum mechanics. The configurations corresponding to minima in the energy surface from the QM calculations do not necessarily agree with minima in the energy surface using the classical potentials with the various sets of point charges.

We examined whether the discrepancies between the QM and classical distributions might be attributed to the use of charge distributions that do not correspond to the system being simulated. We therefore also generated charges from configurations of RDX adsorbed in IRMOF-10. These systems also failed to agree well with binding energies from QM calculations.

For the charge sets studied, the amount of RDX adsorbed tracks with the binding energy but varies over 7 orders of magnitude for the 15 combinations of charges studied here. The self-diffusivities of RDX in IRMOF-10 for each combination simulated are also significantly different.

Interestingly, the QM calculations show that the dispersion contribution is a significant fraction of the binding energy and is substantially larger than any L-J interaction observed in the classical simulations. Therefore, the inability of the classical simulations to reproduce the QM binding energies may in part be attributed to shortcomings of the L-J potential or its parameters in this application and not just the charge distribution. One could increase the dispersion contribution of the L-J potential to better match the QM energies in this work by increasing the well depth, characterized by ϵ . However, this change would impact all of the other properties to which the parameters were originally fit. Although adsorption isotherms for nonpolar molecules like methane in IRMOFs are relatively insensitive to L-J parameters,²³ it appears that this may not be the case for polar molecules like RDX.

The adsorption isotherm of polar molecules in IRMOFs is certainly sensitive to partial charges. However, adjusting partial charges to match an experimental isotherm point may not address the physical issue underlying the discrepancy, if the reason for the discrepancy lies with the dispersion contribution to the interaction energy.

Finally, it is difficult due to the scarcity of experimental data to identify a “best” method for determining charges for polar molecules adsorbed in MOFs. Therefore, additional experimental data are needed (such as points on the isotherm) which could help to resolve key questions, especially that of condensation in the pore.

Acknowledgment. The authors gratefully acknowledge the financial support of National Science Foundation (NSF) under Grant CMMI-0730207. Work at ORNL was performed under the auspices of the Division of Materials Science and Engineering, Office of Basic Energy Science of the US Department of Energy (DMN). Work at ORNL was supported by the Center for Nanophase Materials Sciences, sponsored by the Division of Scientific User Facilities, Office of Basic Energy Science of the US Department of Energy (MFC) and used resources of the National Center for Computational Sciences (NCCS), ORNL, supported by the Office of Science, USDOE, as well as resources of the National Institute for Computational Sciences (NICS), ORNL, supported by NSF with agreement number: OCI 07-11134. This work also used resources of Pittsburgh Supercomputing Center and West Virginia University (WVU) Nano for computing facilities.